

Dynamic approach to finite-temperature magnetic phase transitions in the extended J_1 - J_2 model with a vacancy order

N.J. Zhou^{1*}, B. Zheng², and J.H. Dai¹

¹*Department of Physics, Hangzhou Normal University, Hangzhou 310036, P.R. China*

²*Department of Physics, Zhejiang University, Hangzhou 310027, P.R. China*

Abstract

The recently discovered iron-based superconductors $A_y\text{Fe}_{2-x}\text{Se}_2$ ($A=\text{K, Rb, Cs, Tl}$) show a long-range antiferromagnetic order with an unexpected high transition temperature $T_N \sim 550$ K and a unique $\sqrt{5} \times \sqrt{5}$ vacancy order. Taking the extended J_1 - J_2 model as a minimal model, we investigate the finite-temperature magnetic phase transitions in a square lattice with a $\sqrt{5} \times \sqrt{5}$ vacancy superstructure by using large-scale Monte Carlo simulations. By the parallel tempering technique, the block spin checkerboard and stripe antiferromagnetic states are detected to be the groundstates for three representative sets of model parameters. The short-time dynamic approach is applied to accurately determine the critical temperature as well as the static and dynamic exponents. Our results indicate that the dramatic enhancement of the critical temperature as observed in experiments should be mainly due to a combination effect of the vacancy order and the block lattice contraction.

PACS numbers: 64.60.Ht, 74.25.Ha, 05.10.Ln

* corresponding author; email: zhounengji@hznu.edu.cn

I. INTRODUCTION

The discovery of superconductivity in iron pnictides [1–5] has renewed an intensive study on the interplay between superconductivity and antiferromagnetism [6]. A broad family of the iron-based superconductors has been synthesized, of which the parent compounds are typically represented by the 1111-type LaFeAsO [1], the 122-type BaFe₂As₂ [7], the 111-type LiFeAs [8], and the 11-type FeSe [9]. Antiferromagnetic transitions occur around the Néel temperature $T_N \approx 100 - 200$ K, and the long-range magnetic order is a stripe-like (or collinear) antiferromagnetic state [10, 11] except for the 11-type where the magnetic order is a bi-collinear antiferromagnetic state [12]. The magnetic properties as well as superconductivity are closely related to a common two-dimensional (2D) Fe-atom square lattice [13–15]. The effective magnetic moments of each iron determined in experiments are usually within $0.3\mu_B/\text{Fe} - 1.0\mu_B/\text{Fe}$, while the iron moments estimated from the first-principles calculations [16–19] or model analysis [20] could be around $2.0\mu_B/\text{Fe}$ or larger.

Recently, a new family of iron-based superconductors, i.e., the intercalated iron chalcogenides $A_y\text{Fe}_{2-x}\text{Se}_2$ ($A=\text{K, Rb, Cs, Tl}$), has been found with a moderate high superconducting transition temperature $T_{sc} \sim 30$ K [21–23]. These materials are structurally similar to the 122-type iron pnictides, except that there are certain amounts of Fe-vacancies in the iron square sublattice. The iron vacancies are expected to order in some periodic superstructures, rather than to distribute randomly within the FeSe layer, resulting in the normal state insulating behavior [22]. Indeed, the $\sqrt{5} \times \sqrt{5}$ vacancy ordering pattern as shown in Fig. 1, corresponding to $x = 0.4$, seems to be most stable as confirmed in the neutron diffraction [24–26] and transmission electron microscopy [27] experiments. In addition, a novel magnetic ordering pattern, i.e., block spin checkerboard (BSC) state has also been observed, with an unexpected high transition temperature $T_N \sim 550$ K and a large effective magnetic moment $\sim 3.31\mu_B/\text{Fe}$.

Early theoretical explorations to the magnetic and electronic structures of $A_y\text{Fe}_{1.6}\text{Se}_2$ based on the first-principles calculations have revealed the BSC state as the groundstate with effective iron moment $\sim 2.8\mu_B/\text{Fe} - 3.4\mu_B/\text{Fe}$, and a band gap ~ 500 meV at $y = 0.8$ [28, 29]. Another silent feature is a significant lattice contraction of the fundamental iron blocks but without breaking the symmetry of lattice structure. The observation leads to a microscopic consideration for the magnetic structure based on the extended J_1 - J_2 spin model

[28], where the BSC state could be the groundstate for certain range of model parameters [30]. This model involves the nearest-neighbor (NN) and the next-nearest-neighbor (NNN) exchange interactions, and captures the vacancy superstructure and the lattice distortion in a minimal manner. Other models like the J_1 - J_2 - J_3 spin model, which emphasizes the relaxation of magnetic frustration by the third-nearest-neighbor exchange interaction without [31] or with [32] a biquadratic interaction term, can also account for the BSC state.

Experimentally, the vacancy order and the BSC state coexist with the superconductivity in the $A_y\text{Fe}_{2-x}\text{Se}_2$ compounds for $y \gtrsim 0.8$, $x \lesssim 0.4$. This raises heated debate on whether the co-existence is an intrinsic property of a single phase electronic structure [33] or due to a phase separation [34]. Theoretically, the importance of the vacancy order and the BSC state in the formation of the insulating phase as well as superconductivity has been investigated [32, 35–42]. However, the question that why the magnetic transition temperature T_N is much higher than the ones in other iron pnictides or chalcogenides, has not been addressed so far by detailed calculations.

This fundamental question is actually non-trivial. Firstly, it is believed that unconventional superconductivity, which frequently emerges near the border of antiferromagnetic phases such as in the cuprates, heavy fermions, and iron pnictides/chalcogenides, is usually related to the magnetic fluctuations with a characteristic energy scale roughly proportional to the magnetic transition temperature T_N [43]. But the present class of intercalated iron chalcogenides ($A_y\text{Fe}_{2-x}\text{Se}_2$) is an obvious exception. Secondly, while the intralayer magnetic interactions J_1 and J_2 in $A_y\text{Fe}_{2-x}\text{Se}_2$ are comparable to those in iron pnictides [44] as well as in $A\text{Fe}_2\text{Se}_2$ without vacancies [45, 46], the interlayer magnetic coupling is very small [28] and is not sufficient to account for the enhancement of T_N . Thirdly, it is well-known that uniformly and randomly distributed vacancies in spin systems always lead to a reduction of transition temperatures such as in the randomly site-diluted Ising model [47]. Therefore, detailed calculations are required to understand why and how the opposite tendency could appear in the $A_y\text{Fe}_{2-x}\text{Se}_2$ compounds.

In this paper, we consider this question by performing systematic simulations on the finite-temperature magnetic phase transitions in the extended J_1 - J_2 spin model defined in a square lattice with a $\sqrt{5} \times \sqrt{5}$ vacancy superstructure. This model has a rich phase diagram consisting of numerous groundstates when we tune the model parameters [28, 30]. We then focus on three representative sets of model parameters. Our goals are of two-folds:

to clarify the nature of the finite-temperature magnetic order-disorder phase transitions and to understand the mechanism increasing the transition temperatures. Though the relation between the magnetic transition temperature T_N and the onset of superconductivity is not addressed, our study indicates that the enhancement of the critical temperature may be irrelevant to the superconductivity. In other words, our results favor the phase separation scenario [34].

According to the $\sqrt{5} \times \sqrt{5}$ vacancy superstructure, the concentration of vacancies $p = 20\%$ is considered, corresponding to $x = 0.4$ in realistic $A_y\text{Fe}_{2-x}\text{Se}_2$ compounds with the superconductivity and high magnetic transition temperature. The specified spatial distribution of vacancies as observed in experiments is the simplest vacancy superstructure in a square lattice with the highest symmetry, since all iron atoms are 3-coordinated equivalently.

There are several technique difficulties to our numerical investigations. For the systems with (J_1, J_2) couplings and vacancies, sufficiently large system sizes are required in order to find the true groundstate among numerous possible magnetic configurations. For this purpose, the parallel tempering technique based on Monte Carlo method, which was applied in studying spin glass systems [48], is an appropriate approach. Once the groundstate is determined, the magnetic order-disorder phase transition at finite temperatures can be investigated by large-scale Monte Carlo simulations. However, even for the frustrated Ising model without vacancies, it is difficult to precisely determine the order and the universality class of the phase transitions.[49, 50] In this respect, the short-time dynamic approach [51, 52] can be utilized. Recent activities include various applications and developments [53, 54] such as theoretical and numerical studies of the Josephson-junction arrays [55] and ageing phenomena [56, 57]. Very recently, the depinning transition and the relaxation-to-creep transition in the domain-wall motion have been investigated [58–61]. Usually, two relaxation processes with ordered and disordered initial states are considered in the short-time dynamic approach. However, the groundstate of the present model is not simply ordered and homogeneous, and the standard magnetization does not characterize these relaxation dynamics. Methodologically and technically one needs to develop new concepts.

With the parallel tempering technique and the short-time dynamic approach, we are able to find the true groundstate as well as to accurately determine the transition temperature and critical exponents. In Sec. II, the model and scaling analysis are described, and in Sec. III, the numerical results are presented. Finally, Sec. IV is devoted to the conclusions.

II. MODEL AND SCALING ANALYSIS

A. Model and methods

The extended J_1 - J_2 model is the extension of standard J_1 - J_2 model defined on the Fe-square lattice of iron pnictides [20] to the situation with a Fe-vacancy superstructure. Here, the distance between two NN vacancies is $\sqrt{5}$ in unit of the distance between two NN iron sites. Owing to the $\sqrt{5} \times \sqrt{5}$ vacancy superstructure, the whole lattice consists of the fundamental minimal square blocks containing four iron sites. Due to the symmetry invariant lattice distortion, the intrablock and interblock interactions could be different [28]. The model is then defined by the following Hamiltonian,

$$\begin{aligned}
 H = & \sum_{n,\alpha} (J_1 S_{n,\alpha} S_{n,\alpha+1} + J_2 S_{n,\alpha} S_{n,\alpha+2}) \\
 & + \sum_{n,\alpha} J'_1 S_{n,\alpha_\delta} S_{n+\delta,\alpha_\delta} + \sum_{n,\alpha} J'_2 (S_{n,\alpha_\delta} S_{n+\delta,\alpha_\delta+1} \\
 & + S_{n,\alpha_\delta} S_{n+\delta-1,\alpha_\delta-1}), \tag{1}
 \end{aligned}$$

where n denotes the block index, $n+\delta$ is short for the nearest-neighboring block, α is the site index which goes from 1 to 4, and α_δ selects the site connecting to the nearest-neighboring block. J_1 and J'_1 (J_2 and J'_2) are the NN (NNN) couplings of intra- and interblock, as shown in Fig. 1. Since an almost saturated magnetic moment at the iron site is reported [24], the quantum effect is suppressed at finite temperatures due to the large local spin. So the corrections due to quantum fluctuations to the magnetic properties at finite temperatures can be safely neglected. Therefore, the spin is treated as a classical Ising spin, i.e., $S_{n,\alpha} = \pm 1$. The specific value of $|S|$ is not crucial in the following discussions.

The general phase diagram of this classical J_1 - J_2 spin model is very complicated. A previous Monte Carlo study suggests a phase diagram with several specified groundstates for the vector version of this model with certain model parameters [30]. For our purpose, we consider more simplified cases by fixing the non-zero coupling strengths $|J| = 1$. Explicitly, three representative sets of model parameters are considered,

$$\left\{ \begin{array}{ll} \text{Case-I:} & J_1 = J_2 = -1, \quad J'_1 = J'_2 = 1 \\ \text{Case-II:} & J_1 = J_2 = 1, \quad J'_1 = J'_2 = 1 \\ \text{Case-III:} & J_1 = -1, J_2 = 0, \quad J'_1 = 1, J'_2 = 0 \end{array} \right. . \tag{2}$$

Here, Case-I involves the ferromagnetic intrablock NN and NNN couplings and antiferromagnetic interblock NN and NNN couplings, while all NN and NNN couplings in Case-II are antiferromagnetic. Case-III is a simplification of Case-I, i.e., without the NNN interactions. First-principles calculations suggest that in realistic $A_y\text{Fe}_{2-x}\text{Se}_2$ compounds, J_1 , J_2 , and J'_1 are ferromagnetic, while J'_2 is antiferromagnetic ($J_1 = -43$ meV, $J_2 = -4.5$ meV, $J'_1 = -14.5$ meV, $J'_2 = 19$ meV). However, J'_2 dominates over J'_1 not only because $|J'_2|$ is larger than $|J'_1|$, but also because the number of interblock NNN sites is twice of the interblock NN sites [28]. Thus the sign of J'_1 is not crucial in this case. The origin of the ferromagnetic couplings is a combined effect of Hund's rule coupling and short-ranged hopping integrals (of Fe $3d$ -orbitals and Se $4p$ -orbitals) which are enhanced by the vacancy-induced lattice contraction. Notice that when no iron vacancies appear as such in $A\text{Fe}_2\text{Se}_2$ [45, 46], both NN and NNN interactions are antiferromagnetic as in other iron pnictides.

In the following, we shall find the magnetic configurations of the groundstate and investigate the finite-temperature magnetic order-disorder transitions in each of the three cases with Monte Carlo simulations. To overcome the critical slowing down around the phase transition, we adopt the short-time dynamic approach. Two relaxation processes, i.e., those starting from the groundstate (ordered state) and high-temperature state (disordered state) are considered. To extract the transition temperature and critical exponents, it is more efficient to study the dynamic relaxation starting from the groundstate. Fig. 1 shows two typical magnetic configurations, corresponding to the magnetic ordering patterns of the BSC state and the stripe (or collinear) antiferromagnetic state (denoted by SAFM), as observed in realistic $A_y\text{Fe}_{2-x}\text{Se}_2$ compounds and iron pnictides [10, 24]. We will show that the groundstates of Case-I and Case-II are the BSC and SAFM states, respectively.

For a simple model, such as the Ising model with only NN couplings on a square lattice, it is straightforward to obtain the groundstate magnetic configuration according to the symmetry. However, the vacancy order and frustrated antiferromagnetic NNN interactions in the extended J_1 - J_2 model make this task difficult. Large-scale simulations implemented by the parallel tempering algorithm are then performed to find the true groundstate. The details of the parallel tempering algorithm can be found in Ref.[48], and the main idea is briefly illustrated below. In this algorithm, m parallel replicas are analyzed, each of which is performed independently at a fixed temperature T_j ($T_1 \leq T_j \leq T_m$). Following the reference, we fix $T_1 = 0.1, T_m = 1.6$ and set $T_{j+1} - T_j = (T_m - T_1)/(m - 1)$. In order to avoid the

situation where replicas at low temperatures get stuck in local minima, one can swap the configurations of two randomly selected temperatures T_j and $T_{j'}$. Starting from a random initial condition, a standard Monte Carlo dynamics is performed in each replica, and a trial exchange of two configurations X_j and $X_{j'}$ (corresponding to the j th and j' th replicas) is attempted periodically, and accepted with the probability

$$W(X_j, K_j | X_{j'}, K_{j'}) = \begin{cases} \exp(-\Delta), & \text{for } \Delta > 0 \\ 1, & \text{for } \Delta \leq 0 \end{cases}. \quad (3)$$

Where $\Delta = -(K_j - K_{j'})(H_j - H_{j'})$ is defined with the inverse temperature $K_j = 1/T_j$ and Hamiltonian energy H_j . For convention, we restrict the replica exchange to the case $j' = j+1$. As time evolves, the magnetic configuration at the lowest temperature approaches to the groundstate.

After preparing the groundstate as the initial state, we update the spins with the heat-bath algorithm. Our simulations are performed with lattice sizes $L = 250, 500, \text{ and } 1000$, up to $t_{max} = 25\ 600$ Monte Carlo step (MCS). Here MCS is defined by $L \times L$ single-spin-flips attempts. Different updating schemes, such as the sequential sweep and random sweep, are considered, and yield the same results. Periodic boundary conditions are used along the x and y directions, respectively. For each case, more than 16 000 samples are performed for average. Errors are estimated by dividing the samples into three or four subgroups. If the fluctuation of the curve in the time direction is comparable with or larger than the statistical error, it will be taken into account.

To investigate the dynamic relaxation, the pseudo-magnetization $M(t) \equiv M^{(1)}(t)$ and its second moment $M^{(2)}(t)$ are introduced by the projection to the groundstate,

$$M^{(k)}(t) = \frac{1}{L^{2k}} \left\langle \left[\sum_i S_i(t) X_i \right]^k \right\rangle, \quad k = 1, 2, \quad (4)$$

where $S_i(t)$ is the spin at the time t on the lattice site i , X_i is the one from the groundstate, L is the lattice size, and $\langle \dots \rangle$ represents the thermal average, estimated by the average over samples with different random numbers and initial conditions. The pseudo-magnetization $M(t)$ plays a role as the order parameter of the magnetic transition. When the groundstate is degenerate, a computationally convenient root-mean-square order parameter is introduced [49]. Other important observables are the susceptibility $\chi(t)$ and Binder cumulant $U(t)$,

$$\chi(t) \sim M^{(2)}(t) - M(t)^2,$$

$$U(t) \sim \chi(t)/M(t)^2. \quad (5)$$

For the dynamic relaxation starting from the disordered state, the spatial correlation function $C(r, t)$ and two-time correlation function $A(t, t')$ are measured,

$$\begin{aligned} C(r, t) &= \frac{1}{L^d} \sum_i \langle S_i(t) S_{i+r}(t) \rangle, \\ A(t, t') &= \frac{1}{L^d} \sum_i \langle S_i(t') S_i(t) \rangle, \end{aligned} \quad (6)$$

where r is the spatial distance, t' is the waiting time, and $d = 2$ is the spatial dimension.

B. Scaling analysis

The magnetic order-disorder transition at finite temperatures in the present model is of the second order, compatible with the magnetic transitions in the $A_y\text{Fe}_{2-x}\text{Se}_2$ compounds [24], where no lattice structural transition is accompanied with the magnetic ordering except for the iron vacancy ordering stability taking place at an elevated temperature $T_V \sim 580$ K. Hence, one expects that the order parameter $M(t)$ should obey the dynamic scaling form, after a microscopic time scale t_{mic} [51],

$$M^{(k)}(t, \tau, L) = t^{-k\beta/\nu z} \widetilde{M}(t^{1/\nu z} \tau, t^{1/z}/L), \quad (7)$$

here β and ν are the static exponents, z is the dynamic exponent, and $\tau = (T - T_c)/T_c$ is the reduced temperature. T_c denotes the transition temperature which can be either Curie temperature T_C in the ferromagnetic transition or Néel temperature T_N in the antiferromagnetic transition. On the right side of the equation, the overall factors $t^{-k\beta/\nu z}$ indicates the scaling dimension of $M(t)$, and the scaling function $\widetilde{M}(t^{1/\nu z} \tau, t^{1/z}/L)$ represents the scale invariance of the dynamic system. For a sufficiently large lattice and in the short-time regime, the nonequilibrium spatial correlation length $\xi(t) \sim t^{1/z}$ is much smaller than the lattice size L . Therefore, the finite-size effect is negligible, and a power law behavior is expected at $\tau = 0$,

$$M(t) \sim t^{-\beta/\nu z}. \quad (8)$$

With Eq. (7), the precise location of the transition temperature T_c is determined by searching for the best power-law behavior of $M(t, \tau)$, and the critical exponent $1/\nu z$ is measured from the time derivative of $\ln M(t, \tau)$.

For the susceptibility $\chi(t)$ and Binder cumulant $U(t)$, the scaling behaviors are different. Since $\xi(t)$ is small, the spatially correlating terms $\langle S_1 X_1 S_2 X_2 \rangle$ with $|r_1 - r_2| > \xi(t)$ can be neglected. In other words, one of the two summations over r_1 and r_2 in $M^{(2)}(t) - M(t)^2$ is suppressed. It then leads to the finite-size behaviors $\chi(t), U(t) \sim L^{-d}$. Together with Eqs. (7) and (8), one may derive the scaling forms,

$$\begin{aligned}\chi(t) &\sim t^{\gamma/\nu z}/L^d, \\ U(t) &\sim t^{d/z}/L^d,\end{aligned}\tag{9}$$

with the scaling law $\gamma/\nu = d - 2\beta/\nu$.

For the dynamic relaxation starting from the disordered state, the correlation functions $C(r, t)$ and $A(t, t')$ should obey

$$\begin{aligned}C(r, t) &\sim t^{-2\beta/\nu z} \tilde{C}(r/\xi(t)), \\ A(t, t') &\sim t'^{-2\beta/\nu z} \tilde{A}(\xi(t)/\xi(t')), \end{aligned}\tag{10}$$

where $\tilde{C}(s)$ and $\tilde{A}(q)$ are the scaling functions with $s = r/\xi(t)$ and $q = \xi(t)/\xi(t')$. Together with Eqs. (6) and (10), one may derive the scaling form of the integral $S(t) = \int C(r, t) dr$,

$$S(t) \sim t^{(d_0 - 2\beta/\nu)/z},\tag{11}$$

where d_0 denotes the dimension of the integration. For a sufficiently large lattice and at the critical point T_c , a surprising increasing behavior of the pseudo-magnetization $M(t)$ is observed,

$$M(t) \sim m_0 t^\theta.\tag{12}$$

Here m_0 is the initial magnetization, and θ is a local critical exponent, reflecting the effect of the initial condition [62].

III. MONTE CARLO SIMULATIONS

As shown in Fig. 2(a), the second moment of pseudo-magnetization is displayed in the parallel tempering process at the lowest-temperature replica for Case-I and Case-II. The lattice size $L = 200$ and replica number $m = 10$ are used. As time grows, the curves approach to the unit. It indicates that the BSC and SAFM states, displayed in Fig. 1, are the true groundstates for Case-I and Case-II, respectively. As a test, we also consider a set of

model parameters by re-scaling the couplings obtained from the first-principles calculations [28]. In this case, more than 1 000 samples are performed, up to $t_{max} = 1\,000\,000$ MCS. All of them evolve to the BSC state, reflecting the fact that there is an extended region of the BSC state in the groundstate phase diagram of the model [30].

A. Dynamic relaxation from groundstate

With Monte Carlo simulations, the dynamic relaxation starting from the groundstate is investigated. In Fig. 2(b), the time evolution of the pseudo-magnetization $M(t)$ in Case-I is displayed for different inverse temperatures $K = 1/T$ with the lattice size $L = 500$. The curve drops rapidly down for smaller K , while approaches a constant for larger K . Searching for the best power-law behavior, the critical point $K_c = 0.27595(3)$ is determined accurately. According to Eq. (8), one measures the exponent $\beta/\nu z = 0.0585(6)$ from the slope of the curve at K_c . Additional simulations with $L = 250$ and $L = 1000$ confirm that the finite-size effect is already negligibly small. For comparison, the dynamic behavior in Case-II is also studied, and the critical point $K_c = 0.8148(1)$, the exponent $\beta/\nu z = 0.0556(3)$ are derived.

In order to approximate the differentiation of $\ln M(t, \tau)$, the simulations at temperatures in the vicinity of the critical point are performed. In Fig. 3(a), a power-law behavior of the curves is observed but with certain corrections to scaling at the early times. A direct measurement from the slope gives the exponents 0.471(5) and 0.512(3) for Case-I and II, respectively. After introducing a power-law correction to scaling, $\partial_\tau \ln M(t) \sim t^{1/\nu z}(1 + c/t)$ [57], one can fit the numerical data extending to rather early times. It yields $1/\nu z = 0.468$ in Case-I, and 0.510 in Case-II.

In Fig. 3(b), the time evolution of the Binder cumulant $U(t)$ is plotted at K_c for these two cases. The possible finite-size behavior is also investigated with different lattice sizes $L = 250, 500$ and 1000, and data collapse is observed according to Eq. (9). From the slope, one measures the exponent $d/z = 0.928(5)$ in Case-I, and 0.921(5) in Case-II.

Finally, according to the measurements of $\beta/\nu z$, $1/\nu z$, and d/z , we calculate the individual exponents $\beta = 0.125(2), \nu = 1.00(1), z = 2.16(1)$ in Case-I, and $\beta = 0.109(1), \nu = 0.90(1), z = 2.17(1)$ in Case-II.

B. Dynamic relaxation from disordered state

Now we turn to the dynamic relaxation starting from the disordered state at the critical temperature T_c . In Fig. 4(a), the spatial correlation function $C(r, t)$ is displayed for Case-I as a function of distance r at different time t . To confirm the scaling behavior of $C(r, t)$, for example, we fix $t' = 20480$ MCS, and rescale r to $(t'/t)^{1/z}r$ and $C(r, t)$ to $(t'/t)^{-2\beta/\nu z}C(r, t)$. Data of different t nicely collapse to the curve of t' with the exponents $\beta/\nu z = 0.0585$ and $z = 2.16$ as input. A power-law decay is then observed at small $s = r/\xi(t)$ with the slope $2\beta/\nu = 0.25(1)$. In order to extract the characteristic of the scaling function, $\tilde{C}(s)s^{0.25}$ against s is plotted in the inset. For large s (e.g. $s \geq 2$), an exponential behavior is detected, indicating the scaling form,

$$\tilde{C}(s) \sim s^{-2\beta/\nu} \exp(-\alpha s). \quad (13)$$

Together with Eqs. (10) and (13), one may derive the critical behavior of the spatial correlation function $C(r, t)$ in the limit $r/\xi(t) \rightarrow \infty$,

$$C(r, t) \sim \frac{1}{r^{2\beta/\nu}} \exp(-\alpha r/\xi(t)), \quad (14)$$

here $\xi(t) \sim t^{1/z}$ is the spatial correlation length.

In Fig. 4(b), the integrated correlation function $S(t)$ is displayed for Case-I, and the exponent $(d_0 - 2\beta/\nu)/z = 0.331(8)$ is estimated from the slope, according to Eq. (11). The dimension $d_0 = 0.97(2)$ is calculated, very close to 1. Similarly, a power law behavior is also observed for the susceptibility $\chi(t)$ with the slope $\gamma/\nu z = 0.806(4)$. It yields the exponent $\gamma = 1.72(2)$. While similar measurement for Case-II yields a different value of $\gamma = 1.58(2)$.

The scaling behavior of the two-time correlation function represents a kind of ageing phenomena [56, 57]. According to Eq. (10), the scaling function $\tilde{A}(t/t')$ is plotted in Fig. 5(a), as a function of $q = \xi(t)/\xi(t')$. Obviously, data for different waiting time t' collapse onto a master curve which exhibits a power law decay in the large q regime (e.g. $q \geq 2$). It indicates that the scaling function $\tilde{A}(q)$ takes the form

$$\tilde{A}(q) \sim q^{-\lambda}, \quad (15)$$

with the scaling law $\lambda = d - \theta z$. According to the formula, the critical exponents $\lambda = 1.59(1)$ and $1.65(1)$ are estimated for Case-I and II, respectively.

Finally, a surprising increase of the pseudo-magnetization $M(t)$ is displayed in Fig. 5(b) with the lattice size $L = 1000$. From the slope of the curve, one measures the critical

exponent θ . Strictly speaking, θ is defined at the limit $m_0 \rightarrow 0$. However, practical measurement at this limit is not possible. In this work, the initial magnetization $m_0 = 0.01$ is prepared, which is believed to be small enough. It yields the exponent $\theta = 0.186(2)$ in Case-I, larger than the corresponding value $0.167(1)$ in Case-II.

C. Discussion

All the measurements of the transition temperature and critical exponents are summarized in Table I, in comparison with those of the $2D$ square Ising model without vacancies. In general, the vacancies would lead to a reduction in the transition temperature [47]. Magnetic frustration induced by the antiferromagnetic NNN interaction will also decrease the transition temperature [49]. For example, the calculated critical temperature $T_c = 1/K_c = 1.2273(1)$ in Case-II is much lower than the one 2.2692 in the $2D$ Ising model. The reduction of T_c should be due to both vacancies and magnetic frustration. However, a dramatic enhancement in the transition temperature, $T_c = 3.6238(4)$, is found in Case-I. This value is much larger than that of the $2D$ Ising model, and almost three times as large as that in Case-II. Differences between Case-I and Case-II are also observed in individual critical exponents $\beta, \nu, \gamma, \theta$, and λ which differ by about 10%. It suggests that the magnetic transitions in Case-I and Case-II are not in the same universality class. Further comparison shows that the former belongs to the Ising universality class, while the latter does not. Interestingly, the ratios $\beta/\nu, \gamma/\nu$, and the dynamic exponent z in Case-II agree well with the corresponding values of the $2D$ Ising model. It supports the dynamic generalization of the "weak universality" hypothesis proposed by Suzuki [49, 63], where only the reduced critical exponents $\beta/\nu, \gamma/\nu$ and $z = \Delta/\nu$ are universal, irrelevant to the details of the interactions.

In order to understand above results, a simpler example, Case-III defined in Eq. (2), is investigated. Using the parallel tempering algorithm, the BSC state is confirmed as the groundstate, too. In Fig. 6(a), the inverse transition temperature $K_c = 0.6952(1)$ and the exponent $\beta/\nu z = 0.0564(4)$ are measured from the dynamic relaxation from the groundstate. Other critical exponents are also calculated, as shown in Table. I. Except for the transition temperature, the critical exponents in both Case-I and Case-III are very close to the ones of the $2D$ Ising model, showing that they are both in the Ising universality.

Now we argue that the agreement of critical exponents for Case-I, Case-III and the $2D$

Ising model is not an accident. The present model, though with vacancies, has a perfect symmetry that each site has three equivalent neighbors preserving both $\sqrt{5} \times \sqrt{5}$ translational and four-fold rotational invariances of the lattice structure [41]. In particular, Case-III is invariant under a *block-spin rotation*: $S_i \rightarrow S_i e^{in\pi}$, associated with a mapping $J_1 \rightarrow J_1$, $J'_1 \rightarrow -J'_1$. Here, the integer n denotes the block index, and J_1 (J'_1) indicates the coupling of intrablock (interblock). Therefore, the model is equivalent to the ferromagnetic Ising model defined on the square lattice with the vacancy superstructure. Then, a topological deformation can be performed from the square lattice with the $\sqrt{5} \times \sqrt{5}$ vacancy order to the bathroom-tile lattice, as illustrated in Fig. 6(b). Hence Case-III and the 2D bathroom-tile ferromagnetic Ising model are equivalent. Remarkably, the latter model (with the NN coupling only) is exactly solvable, with the exact inverse Curie temperature $K_c = \tanh^{-1}(\sqrt{(5 + 4\sqrt{2})/2} - 1 - 1/\sqrt{2}) \approx 0.6951$ [64]. This value is in perfect agreement with our numerical value 0.6952(1) of Case-III. In addition, it is known that the Ising models defined on the square, triangular, Kagome, and bathroom-tile lattices belong to the same universality class [51, 65–68]. As a consequence, identical critical exponents are predicted between Case-III and the 2D Ising model, as revealed in our numerical results. We note that the critical temperature T_c is lower in Case-III than in the 2D Ising mode. This is clearly due to the existence of vacancies (with the concentration 20%, corresponding to $x = 0.4$ in realistic $A_y\text{Fe}_{2-x}\text{Se}_2$ compounds), which in turn leads to three NN bonds for each iron site.

Similar analysis can also be carried out for Case-I and Case-II. Under the block-spin rotation and the topological transformation, the bathroom-tile Ising model with both the ferromagnetic NN and NNN couplings is derived from Case-I. Since the ferromagnetic NNN coupling is irrelevant to the Ising universality, the critical exponents agree well with those of the 2D Ising model. However, it significantly enhances the transition temperature T_c due to the increase of the ferromagnetic coupled bonds. By contrast, the situation is quite different in Case-II, because the magnetic frustration between the antiferromagnetic NN and NNN couplings exists still even after the mapping. It explains why the individual exponents are non-universal (may vary with model parameters in the same SAFM phase) and different to those of the 2D Ising model. Meanwhile, the transition temperature T_c is also suppressed.

We note that for the parameters obtained from the first-principles calculations, i.e., $J_1 = -43$ meV, $J_2 = -4.5$ meV, $J'_1 = -14.5$ meV, and $J'_2 = 19$ meV [28], above mapping leads to dominating ferromagnetic couplings and small antiferromagnetic cou-

plings. Therefore, the magnetic frustration is actually suppressed in realistic $A_y\text{Fe}_{2-x}\text{Se}_2$ compounds, indicating that they are in the same BSC phase as Case-I. In order to directly compare with experiments, additional simulations are performed with these model parameters. As expected, the transition temperature $T_N = 545\text{K}$ is determined, compatible with the experimental result $T_N \sim 550\text{K}$, and all of the critical exponents, such as $\beta = 0.121(2)$, $\nu = 0.98(1)$, $z = 2.16(1)$, $\theta = 0.189(2)$, $\gamma = 1.69(2)$, and $\lambda = 1.59(1)$, are in good agreement with those in Case-I.

IV. CONCLUSION

Using the parallel tempering technique and short-time dynamic approach, we have numerically investigated the finite-temperature magnetic phase transitions in the extended J_1 - J_2 Ising spin lattice with the $\sqrt{5} \times \sqrt{5}$ vacancy superstructure, for Case-I, Case-II, and Case-III, defined in Eq. (2). The vacancy concentration $p = 20\%$ is considered in the simulations, and results including the transition temperature and critical exponents are summarized in Table I.

(i) The magnetic configuration of the groundstate in Case-I is detected to be the BSC state as observed in realistic $A_y\text{Fe}_{2-x}\text{Se}_2$ compounds with $x \sim 0.4$. While the groundstate magnetic configuration in Case-II is the SAFM state as observed in other iron pnictides without iron vacancies.

(ii) A dramatic enhancement in the transition temperature, $T_c = 3.6238(4)$, is determined in Case-I. This value is almost three times as large as that in Case-II where $T_c = 1.2273(1)$. It is quite compatible with the corresponding magnetic transition temperatures of the BSC ($T_N \sim 550\text{ K}$) [24, 25] and SAFM ($T_N \sim 100 - 200\text{ K}$) [10, 11] phases reported respectively in experiments.

(iii) The nature of the magnetic transition in Case-I is revealed of the $2D$ Ising universality class, while the deviation of the critical exponents from those in the $2D$ Ising model, reaching about 10%, indicates that Case-II belongs to the Suzuki's weak universality class.

(iv) Case-III is shown to be equivalent to the bathroom-tile Ising model which is exactly solvable. Good agreement between the numerical results and the exact solution demonstrates the validity of our numerical simulations on this class of complex systems.

Basing on these numerical results, we conclude that the dramatic enhancement of the

transition temperature in the BSC state as observed in realistic materials $A_y\text{Fe}_{2-x}\text{Se}_2$ should be mainly due to a combination effect of the perfect vacancy superstructure and the block lattice contraction. The latter in turn leads to the suppression of magnetic frustrations due to the ferromagnetic intrablock couplings and the dominating antiferromagnetic interblock NNN coupling. It is also supported by the numerical simulations with the model parameters obtained from the first-principles calculations, where the transition temperature $T_N = 545$ K is compatible with the experimental results $T_N \sim 550$ K.

Acknowledgements: We would like to thank helpful discussions with C. Cao. This work was supported in part by the National Natural Science Foundation of China (under Grant Nos. 11205043, 11075137 and 11274084).

-
- [1] Y. Kamihara, T. Watanabe, M. Hirano, and H. Hosono, *J. Am. Chem. Soc.* **130**, 3296 (2008).
 - [2] X.H. Chen, T. Wu, R.H. Liu, H. Chen, and D.F. Fang, *Nature* **453**, 761 (2008).
 - [3] G.F. Chen, Z. Li, D. Wu, G. Li, W.Z. Hu, J. Dong, P. Zheng, J.L. Luo, and N.L. Wang, *Phys. Rev. Lett.* **100**, 247002 (2008).
 - [4] Z.A. Ren, W. Lu, J. Yang, W. Yi, X.L. Shen, C. Zheng, G.C. Che, X.L. Dong, L.L. Sun, F. Zhou, and Z.X. Zhao, *Chin. Phys. Lett.* **25**, 2215 (2008).
 - [5] C. Wang, L.J. Li, S. Chi, Z.W. Zhu, Z. Ren, Y.K. Li, Y.T. Wang, X. Lin, Y.K. Luo, S. Jiang, X.F. Xu, G.H. Cao, and Z.A. Xu, *Europhys. Lett.* **83**, 67006 (2008).
 - [6] J. Paglione and R.L. Greene, *Nature Phys.* **6**, 645 (2010).
 - [7] M. Rotter, M. Tegel, and D. Johrendt, *Phys. Rev. Lett.* **101**, 107006 (2008).
 - [8] X.C. Wang, Q.Q. Liu, Y.X. Lv, W.B. Gao, L.X. Yang, R.C. Yu, F.Y. Li, and C.Q. Jin, *Solid State Commun.* **148**, 538 (2008).
 - [9] F.C. Hsu, J.Y. Luo, K.W. Yeh, T.K. Chen, T.W. Huang, P.M. Wu, Y.C. Lee, Y.L. Huang, Y.Y. Chu, D.C. Yan, and M.K. Wu, *Proc. Natl. Acad. Sci. U.S.A.* **105**, 14262 (2008).
 - [10] C. de la Cruz, Q. Huang, J.W. Lynn, J.Y. Li, W. Ratcliff II, J.L. Zarestky, H.A. Mook, G.F. Chen, J.L. Luo, N.L. Wang, and P.C. Dai, *Nature* **453**, 899 (2008).
 - [11] H. Chen, Y. Ren, Y. Qiu, W. Bao, R.H. Liu, G. Wu, T. Wu, Y.L. Xie, X.F. Wang, Q. Huang, and X.H. Chen, *Europhys. Lett.* **85**, 17006 (2009).
 - [12] W. Bao, Y. Qiu, Q. Huang, M.A. Green, P. Zajdel, M.R. Fitzsimmons, M.Zhernenkov, S.

- Chang, M.H. Fang, B. Qian, E.K. Vehstedt, J.H. Yang, H.M. Pham, L. Spinu, and Z.Q. Mao, Phys. Rev. Lett. **102**, 247001 (2009).
- [13] D.J. Singh, Physica C: Superconductivity **469**, 418 (2009).
- [14] D.C. Johnston, Advances in Physics **59**, 803 (2010).
- [15] I. Mazin, Physics **4**, 26 (2011).
- [16] D.J. Singh and M.H. Du, Phys. Rev. Lett. **100**, 237003 (2008).
- [17] C. Cao, P.J. Hirschfeld, and H.P. Cheng, Phys. Rev. **B 77**, 220506(R) (2008).
- [18] T. Yildirim, Phys. Rev. Lett. **101**, 057010 (2008).
- [19] F.J. Ma, Z.Y. Lu, and T. Xiang, Phys. Rev. **B 78**, 224517 (2008).
- [20] Q.M. Si and E. Abrahams, Phys. Rev. Lett. **101**, 076401 (2008).
- [21] J.G. Guo, S.F. Jin, G. Wang, S.C. Wang, K.X. Zhu, T.T. Zhou, M. He, and X.L. Chen, Phys. Rev. **B 82**, 180520(R) (2010).
- [22] M.H. Fang, H.D. Wang, C.H. Dong, Z.J. Li, C.M. Feng, J. Chen, and H.Q. Yuan, Europhys. Lett. **94**, 27009 (2011).
- [23] H.D. Wang, C.H. Dong, Z.J. Li, Q.H. Mao, S.S. Zhu, C.M. Feng, H.Q. Yuan, and M.H. Fang, Europhys. Lett. **93**, 47004 (2011).
- [24] W. Bao, Q.Z. Huang, G.F. Chen, M.A. Green, D.M. Wang, J.B. He, and Y.M. Qiu, Chin. Phys. Lett. **28**, 086104 (2011).
- [25] F. Ye, S. Chi, W. Bao, X.F. Wang, J.J. Ying, X.H. Chen, H.D. Wang, C.H. Dong, and M.H. Fang, Phys. Rev. Lett. **107**, 137003 (2011).
- [26] V.Y. Pomjakushin, E.V. Pomjakushina, A.K. Maziopa, K. Conder, and Z. Shermadini, J. Phys. Cond. Mat. **23**, 156003 (2011).
- [27] Z. Wang, Y.J. Song, H.L. Shi, Z.W. Wang, Z. Chen, H.F. Tian, G.F. Chen, J.G. Guo, H.X. Yang, and J.Q. Li, Phys. Rev. **B 83**, 140505(R) (2011).
- [28] C. Cao and J.H. Dai, Phys. Rev. Lett. **107**, 056401 (2011).
- [29] X.W. Yan, M. Gao, Z.Y. Lu, and T. Xiang, Phys. Rev. **B 83**, 233205 (2011).
- [30] R. Yu, P. Goswami, and Q.M. Si, Phys. Rev. **B 84**, 094451 (2011).
- [31] C. Fang, B. Xu, P.C. Dai, T. Xiang, and J.P. Hu, Phys. Rev. **B 85**, 134406 (2012).
- [32] J.P. Hu, B. Xu, W.M. Liu, N.N. Hao, and Y.P. Wang, Phys. Rev. **B 85**, 144403 (2012).
- [33] R.H. Liu, X.G. Luo, M. Zhang, A.F. Wang, J.J. Ying, X.F. Wang, Y.J. Yan, Z.J. Xiang, P. Cheng, G.J. Ye, Z.Y. Li, and X.H. Chen, Europhys. Lett. **94**, 27008 (2011).

- [34] F. Chen, M. Xu, Q.Q. Ge, Y. Zhang, Z.R. Ye, L.X. Yang, J. Jiang, B.P. Xie, R.C. Che, M. Zhang, A.F. Wang, X.H. Chen, D.W. Shen, J.P. Hu, and D.L. Feng, *Phys. Rev.* **X 1**, 021020 (2011).
- [35] C. Cao and J.H. Dai, *Phys. Rev.* **B 83**, 193104 (2011).
- [36] X.W. Yan, M. Gao, Z.Y. Lu, and T. Xiang, *Phys. Rev. Lett.* **106**, 087005 (2011).
- [37] R. Yu, J.X. Zhu, and Q. Si, *Phys. Rev. Lett.* **106**, 186401 (2011).
- [38] Y. Zhou, D.H. Xu, F.C. Zhang, and W.Q. Chen, *Europhys. Lett.* **95**, 17003 (2011).
- [39] F. Wang, F. Yang, M. Gao, Z.Y. Lu, T. Xiang, and D.H. Lee, *Europhys. Lett.* **93**, 57003 (2011).
- [40] G.M. Zhang, Z.Y. Lu, and T. Xiang, *Phys. Rev.* **B 84**, 052502 (2011).
- [41] H. Chen, C. Cao, and J.H. Dai, *Phys. Rev.* **B 83**, 180413(R) (2011).
- [42] H.M. Jiang, W.Q. Chen, Z.J. Yao, and F.C. Zhang, *Phys. Rev.* **B 85**, 104506 (2012).
- [43] D.J. Scalapino, arXiv:1207.4093, to appear in *Rev. Mod. Phys.* (2012).
- [44] M.Y. Wang, C. Fang, D.X. Yao, G.T. Tan, L.W. Harriger, Y. Song, T. Netherton, C.L. Zhang, M. Wang, M.B. Stone, W. Tian, J.P. Hu, and P.C. Dai, *Nat. Commun.* **2**, 580 (2011).
- [45] X.W. Yan, M. Gao, Z.Y. Lu, and T. Xiang, *Phys. Rev.* **B 84**, 054502 (2011).
- [46] C. Cao and J.H. Dai, *Chin. Phys. Lett.* **28**, 057402 (2011).
- [47] R. Kenna and J.J. Ruiz-Lorenzo, *Phys. Rev.* **E 78**, 031134 (2008).
- [48] F. Romá, S.R. Gusman, A.J.R. Pastor, F. Nieto, and E.E. Vogel, *Physica A* **388**, 2821 (2009).
- [49] J.Q. Yin and D.P. Landau, *Phys. Rev.* **E 80**, 051117 (2009).
- [50] S.B. Jin, A. Sen, and A.W. Sandvik, *Phys. Rev. Lett.* **108**, 045702 (2012).
- [51] B. Zheng, *Int. J. Mod. Phys.* **B12**, 1419 (1998).
- [52] H.J. Luo, L. Schülke, and B. Zheng, *Phys. Rev. Lett.* **81**, 180 (1998).
- [53] Y. Ozeki and N. Ito, *J. Phys. A: Math. Theor.* **40**, R149 (2007).
- [54] E.V. Albano, M.A. Bab, G. Baglietto, R.A. Borzi, T.S. Grigera, E.S. Loscar, D.E. Rodríguez, M.L.R. Puzzo, and G.P. Saracco, *Rep. Prog. Phys.* **74**, 026501 (2011).
- [55] E. Granato and D. Domínguez, *Phys. Rev* **B 71**, 094521 (2005).
- [56] P. Calabrese and A. Gambassi, *J. Phys. A* **38**, R133 (2005).
- [57] X.W. Lei and B. Zheng, *Phys. Rev.* **E75**, 040104 (2007).
- [58] N.J. Zhou, B. Zheng, and Y.Y. He, *Phys. Rev.* **B80**, 134425 (2009).
- [59] N.J. Zhou, B. Zheng, and D.P. Landau, *Europhys. Lett.* **92**, 36001 (2010).

- [60] N.J. Zhou and B. Zheng, Phys. Rev. **E82**, 031139 (2010).
- [61] X.P. Qin, B. Zheng, and N.J. Zhou, J. Phys. A: Math. Theor. **45**, 115001 (2012).
- [62] H.K. Janssen, B. Schaub, and B. Schmittmann, Z. Phys. **B 73**, 539 (1989).
- [63] S. Tang and D.P. Landau, Phys. Rev. **B 36**, 567 (1987).
- [64] A. Codello, J. Phys. A: Math. Theor. **43**, 385002 (2010).
- [65] Z.H. Luo, L. Mushtaq, Y. Liu, and J.R. Lin, Chin. Phys. **B 18**, 2696 (2009).
- [66] Y.L. Loh, D.X. Yao, and E.W. Carlson, Phys. Rev. **B 77**, 134402 (2008).
- [67] R.J. Baxter and T.C. Choy, J. Phys. A: Math. Gen. **21**, 2143 (1988).
- [68] A. Malakis, G. Gulpinar, Y. Karaaslan, T. Papakonstantinou, and G. Aslan, Phys. Rev. **E 85**, 031146 (2012).

TABLE I: The inverse transition temperatures and critical exponents obtained with the short-time dynamic approach are listed for Case-I, Case-II, and Case-III, in comparison with those of $2D$ Ising model on the square lattice from literatures [51, 54, 57]. Not all of the critical exponents are independent, and the scaling laws $\gamma/\nu + 2\beta/\nu = d$ and $\lambda + \theta z = d$ hold quite well within error bars in each case.

		Case-I	Case-II	Case-III	$2D$ Ising
Ground-state	K_c	0.27595(3)	0.8148(1)	0.6952(1)	0.44069
	β	0.125(2)	0.109(1)	0.122(2)	1/8
	ν	1.00(1)	0.90(1)	1.00(2)	1
	z	2.16(1)	2.17(1)	2.18(2)	2.16(1)
	β/ν	0.125(2)	0.121(2)	0.122(3)	1/8
Disordered	θ	0.186(2)	0.167(1)	0.189(1)	0.191(1)
	γ	1.72(2)	1.58(2)	1.76(3)	7/4
	γ/ν	1.74(2)	1.75(2)	1.77(2)	7/4
	λ	1.59(1)	1.65(1)	1.60(1)	1.59(1)

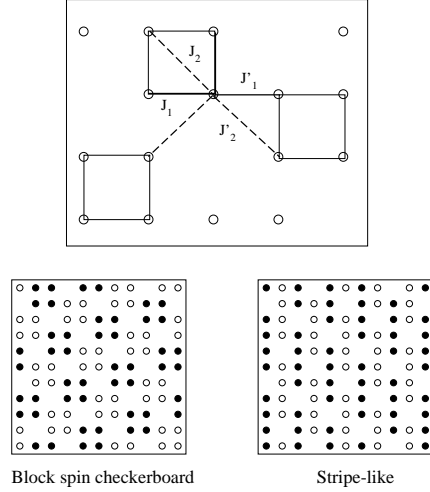


FIG. 1: The magnetic structure of $A_y\text{Fe}_{2-x}\text{Se}_2$ from top-view is displayed. In the upper panel, the solid squares connecting the circles indicate the fundamental blocks with four Fe atoms at the corners. The proposed magnetic couplings (J_1, J'_1) with solid lines and (J_2, J'_2) with dashed lines represent the NN and NNN couplings, respectively. In the lower panel, two magnetic configurations, the block spin checkerboard and stripe-like antiferromagnetic states, are shown by open ($S_i = 1$) and solid circles ($S_i = -1$).

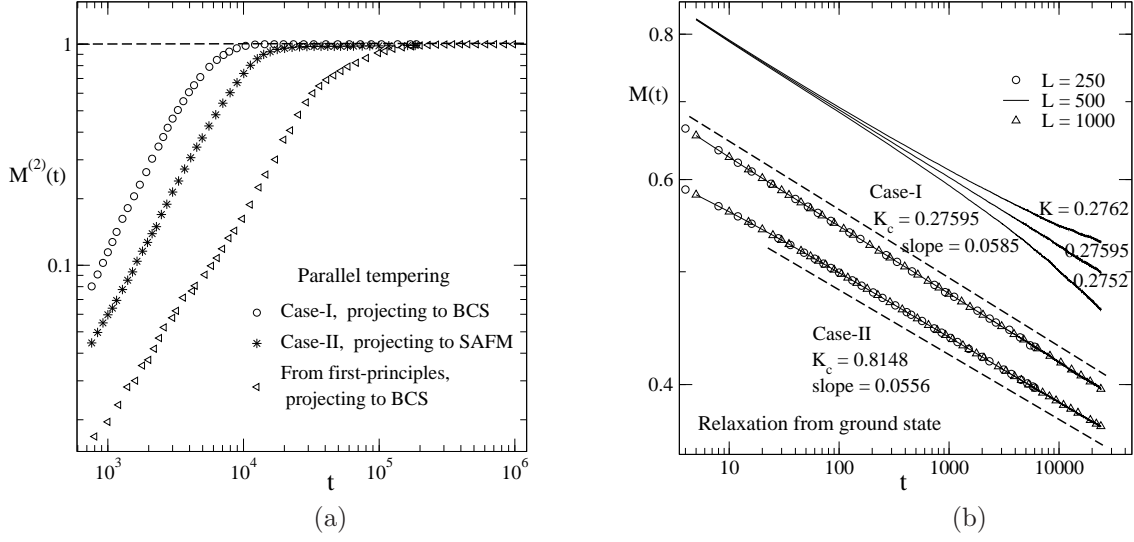


FIG. 2: (a) The second moment of the pseudo-magnetization in the parallel tempering process is displayed for different sets of model parameters. Dashed line represents constant, $M^{(2)}(t) = 1$. (b) Dynamic relaxation of the pseudo-magnetization is plotted for different temperatures. For clarity, the curves at K_c with different lattice sizes are shifted down. Dashed lines indicate power-law fits.

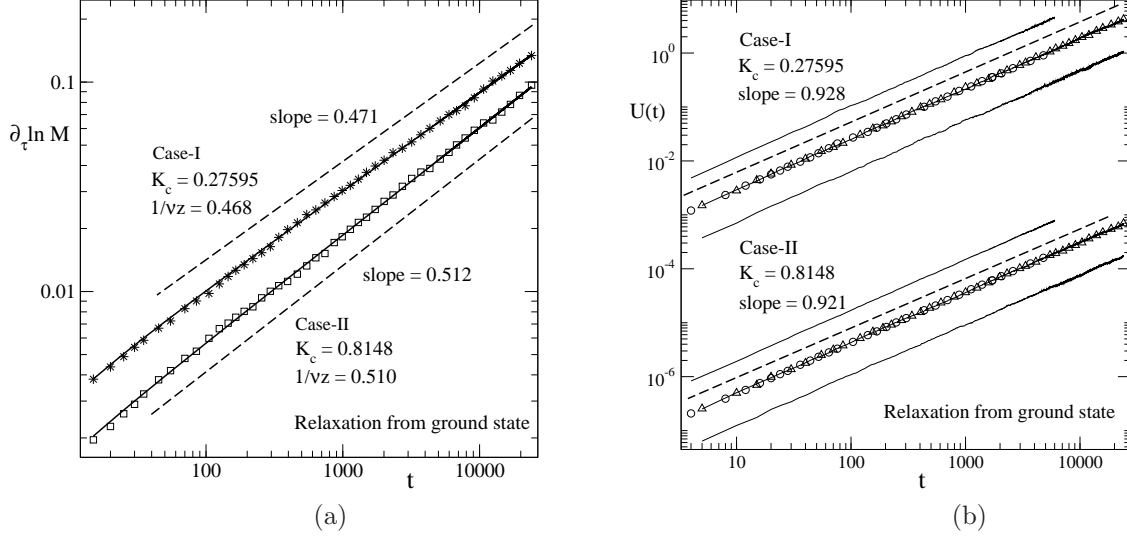


FIG. 3: (a) The logarithmic derivative of the pseudo-magnetization $M(t, \tau)$ is displayed at K_c for Case-I (stars) and Case-II (open squares). Dashed lines represent power-law fits, and solid lines indicate the fits with power-law correction. (b) The Binder cumulant $U(t)$ is plotted with solid lines on a double-log scale for different lattice size $L = 250, 500$ and 1000 (from above). According to Eq. (9), data collapse is demonstrated at a fixed lattice size $L = 500$. Open circles and triangles correspond to $L = 250$ and 1000 , respectively.

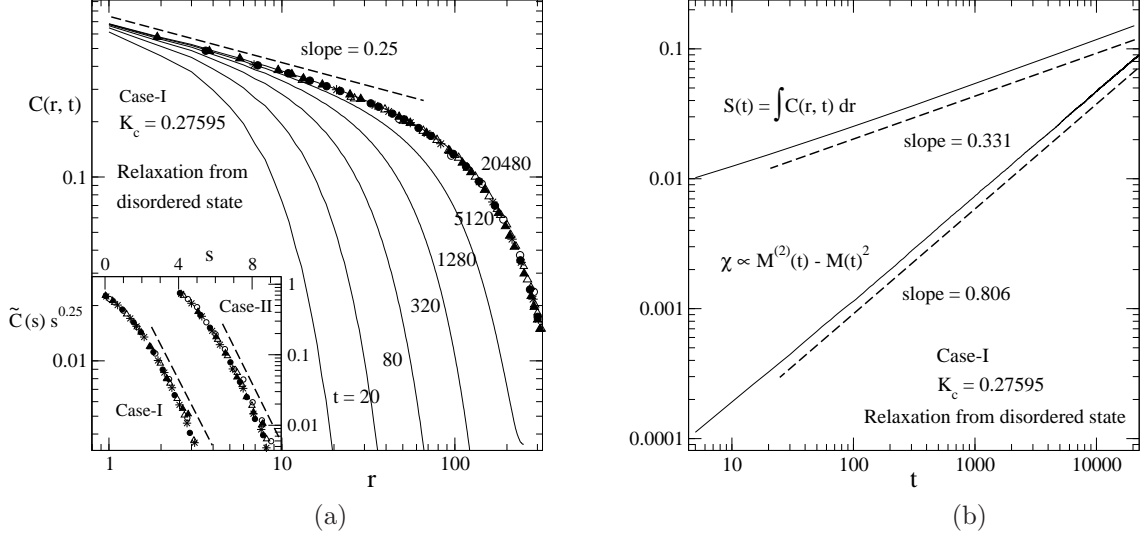


FIG. 4: (a) The spatial correlation function $C(r, t)$ is displayed on a log-log scale. Data collapse is demonstrated at a fixed $t = 20480$ MCS. Open circles, open triangles, stars, solid circles, and solid squares correspond to $t = 20, 80, 320, 1280,$ and 5120 , respectively. In the inset, the scaling function $\tilde{C}(s)s^{0.25}$ is shown on a linear-log scale. For clarity, the curve of Case-II is shifted right. (b) Dynamic relaxation of $\chi(t)$ and $S(t)$ are plotted with solid lines for Case-I. Dashed lines represent

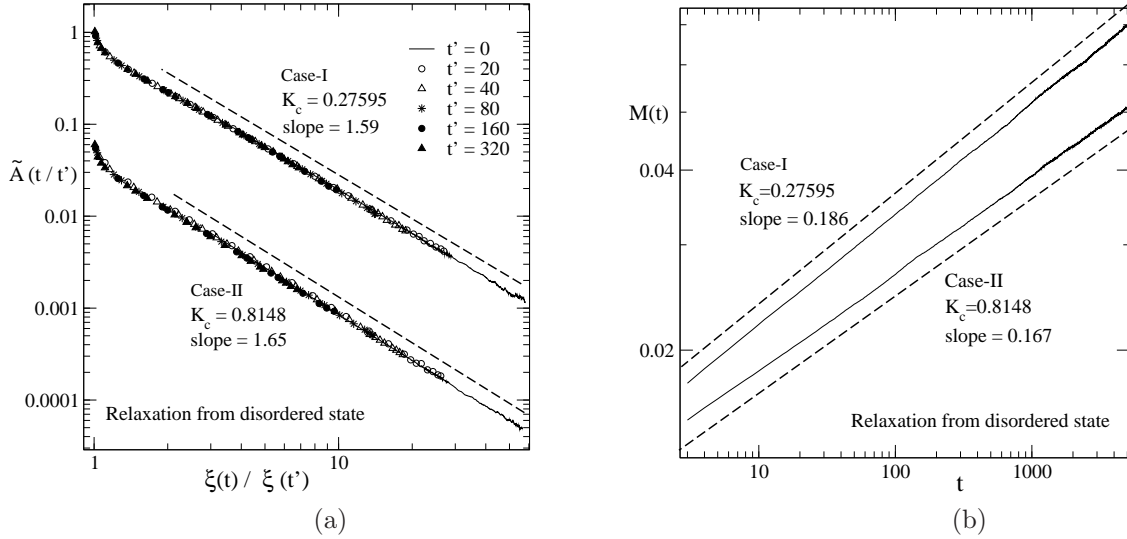


FIG. 5: (a) The scaling function $\tilde{A}(t/t')$ against $\xi(t)/\xi(t')$ is displayed for Case-I and II on a double-log scale. According to Eq. (10), data collapse is observed for different waiting time t' . (b) The time evolution of $M(t)$ is plotted for Case-I and II with an initial magnetization $m_0 = 0.01$. The lattice size is $L = 1000$. In both (a) and (b), dashed lines show power-law fits.

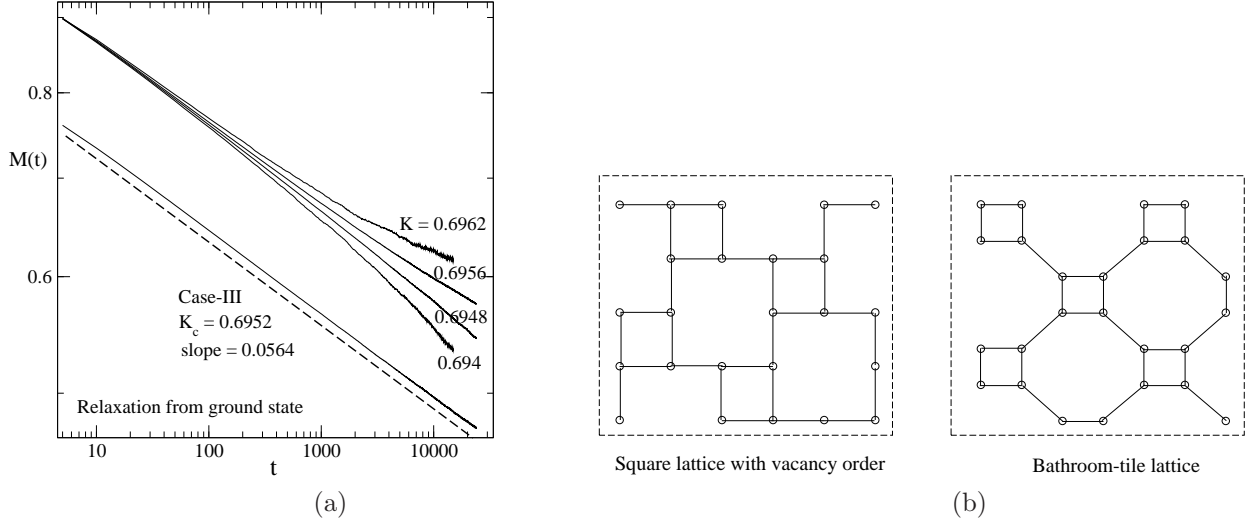


FIG. 6: (a) $M(t)$ in Case-III is plotted for different temperatures. For clarity, the curve at K_c is shifted down. Dashed line shows a power-law fit. (b) The square lattice with a $\sqrt{5} \times \sqrt{5}$ vacancy superstructure and the bathroom-tile lattice are shown within the dashed squares. A same topological structure is revealed.